

Hybrid Liquid Organic Scintillator and Lithium-6 Glass Neutron Detector:

Correlated Pulses

Andrew McClellan

A senior thesis submitted to the faculty of
Brigham Young University
in partial fulfillment of the requirements for the degree of

Bachelor of Science

Lawrence Rees, Advisor

Department of Physics and Astronomy

Brigham Young University

April 2016

Copyright © 2016 Andrew McClellan

All Rights Reserved

ABSTRACT

Hybrid Liquid Organic Scintillator and Lithium-6 Glass Neutron Detector: Correlated Pulses

Andrew McClellan
Department of Physics and Astronomy, BYU
Bachelor of Science

In recent years, there has been a ^3He shortage, resulting in a need for alternative neutron detectors that can efficiently distinguish between neutrons and gammas. A hybrid liquid organic scintillator and lithium-6 glass neutron detector has been developed and tested to determine its neutron-gamma discrimination capabilities using pulse shape discrimination (PSD). Two liquid scintillators, Eljen EJ-325a and EJ-325UV, were compared. The EJ-325UV lacks a wavelength-shifting phosphor so as to minimize the significance of the absorption of lithium glass light in the scintillator. Principal component analysis (PCA) is explored as a method to improve neutron and gamma region separation. Previous work is extended from single- to correlated-pulse analysis, which declares an event a neutron if a liquid scintillator recoil pulse precedes a lithium capture pulse. It was found that PCA fails to improve region separation and efficiencies, but it does provide quantifiable measures of the significance of PSD parameters in distinguishing between events. The correlated-pulse analysis method reduces the ratio of misidentified gammas by an order of magnitude, but reduces the detector efficiency to less than one percent. The detector utilizing EJ-325UV identified 20–40% more neutrons than the EJ-325a detector. Further analysis is needed to determine the importance of self-absorption in the hybrid detector.

Keywords: neutron detector, correlated pulses, scintillator, liquid organic scintillator, lithium-6 glass, pulse shape discrimination, principal component analysis, EJ-325a, EJ-325UV, AST GS20

ACKNOWLEDGMENTS

I would like to thank Dr. Lawrence Rees for all of the time he spent advising me and answering my questions about the project, and for the time spent outside of scheduled meetings doing so. I would also like to thank John Ellsworth for providing technical advice concerning the detector design and electrical setup and other insights. Also, I am grateful for Greg Hill's work assembling the detector and for all the work he did running experiments, writing analysis code, analyzing data, and for the discussions we had that helped further our research.

Last, but certainly not least, I would like to thank my wife, Keturah, for putting up with the late nights spent writing this thesis and for her continual support in my endeavors. All of this would have been impossible without her.

This research has been funded in part by NNSA Grant no. DE-FG52-10NA29655 and DHS Award no. 2010-DN-077-ARI039-02.

Contents

Table of Contents	iv
List of Figures	vi
List of Tables	vii
1 Introduction	1
1.1 Detecting neutral particles	1
1.2 Scintillators	2
1.2.1 Liquid organic scintillators	3
1.2.2 Lithium-6 glass scintillators	3
1.2.3 Comparing liquid organic and lithium-6 glass scintillators	4
1.3 Pulse shape discrimination	5
1.4 Previous and current work	7
1.4.1 Cadmium capture-gated neutron detector	7
1.4.2 Dual PMT lithium-cadmium neutron detector	7
1.4.3 Hybrid liquid organic scintillator and lithium-6 glass detector: single-pulse analysis	7
1.5 Overview	9
2 Experimental and analytical methods	10
2.1 Experimental methods	10
2.1.1 Detector design	10
2.1.2 Equipment and setup	13
2.1.3 Radioactive sources	15
2.2 Analytical methods	16
2.2.1 Pulse shape discrimination	16
2.2.2 Principal component analysis	19
2.2.3 Feature and Fisher weighting	21
2.2.4 Correlated pulses	22
2.2.5 Efficiency calculations	27

3	Results	29
3.1	Statistical analysis	29
3.1.1	Principal component analysis	29
3.1.2	Feature and Fisher weighting	33
3.2	Correlated pulses	36
3.3	Analysis	38
3.4	Conclusions	40
3.5	Further work	41
	Bibliography	44
	Index	47

List of Figures

1.1	High-energy gamma and low-energy neutron overlap region	6
1.2	Lithium-6 and liquid scintillator regions	8
2.1	Peak distributions at 2.5 and 4.0 cm mineral oil depths	11
2.2	Hybrid liquid organic scintillator and lithium-6 glass detector schematic	12
2.3	Electronics schematic	14
2.4	PSD area divisions	17
2.5	Correlated pulses region reference	23
2.6	Correlated pulses region reference: inset	24
2.7	Fraction early vs. total area: after-peaking regions	25
2.8	Example of correlated pulses	26
3.1	Principal PSD plots	31
3.2	^{252}Cf principal axes 1 and 2	32
3.3	Feature and Fisher weighting reference	33

List of Tables

2.1	Radioactive sources	15
2.2	PSD parameters	18
3.1	PCA eigenvalues and eigenvectors	30
3.2	Feature and Fisher weights	34
3.3	PCA with feature weights: eigenvalues and eigenvectors	35
3.4	Calculated efficiencies of EJ-325UV and EJ-325a detectors	37

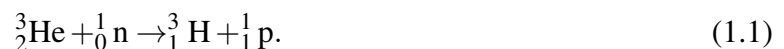
Chapter 1

Introduction

1.1 Detecting neutral particles

Detecting neutral particles presents a challenge. Magnetic and electric fields deflect charged particles and cloud chambers employ gases that condense when charged particles pass nearby, both allowing for direct measurement. However, neither method observes neutrons as they interact with the environment nor provides information regarding the neutron energies present. Neutrons also may penetrate materials to depths of many centimeters without interacting [1], complicating their detection.

One solution to this problem is the helium-3 proportional counter. The helium-3 detector utilizes a chamber filled with this and possibly other gases. An electric field is then applied. The helium-3 captures the neutron in the following reaction:



The protons accelerate in the field, many colliding with other gas molecules and ionizing them. This ion cascade amplifies the original charge of the reaction products, providing a measurable

electrical pulse and indicating that a neutron interacted in the detector [1].

Helium-3 boasts a high cross section for slow (i.e. low-energy) neutrons [1], making it an ideal material for those interested in low-energy neutrons. In many detectors, low-energy neutrons are difficult to distinguish from other forms of radiation. Helium-3 detectors are also used at the United States borders, where they are used to search for illicit radioactive materials [2]. Unfortunately, this increased usage of helium-3 for security and other purposes has changed a surplus into a shortage, and has increased the cost of helium-3 from \$100 to \$2000 per liter [2]. Increasing costs and decreasing supply have encouraged research into alternative methods of neutron detection.

1.2 Scintillators

One class of detector that can replace helium-3 detectors utilizes scintillating materials, called scintillators. These materials convert the kinetic energy of charged particles into light, which is amplified using photomultiplier tubes (PMTs) [1]. There are many different interactions that cause scintillation to occur. For gamma rays, light is produced through Compton scattering. The electrons produced in the scattering travel through the material, inducing transitions between energy states that produce the light detected [1]. Neutrons produce light in some materials by colliding with molecules, which releases photons when it decays from the excited state [1]. The resultant pulse of light is called a recoil pulse. Another common interaction is neutron capture, which causes the nucleus capturing the neutron to decay into charged particles. These charged particles then induce transitions through a process similar to that of the Compton electrons [1].

Scintillators are loosely grouped into two classes: organic and inorganic. The organic scintillators are materials consisting of large amounts of hydrocarbons, while inorganic materials do not contain those molecules [1]. In this work, we use an organic scintillator and an inorganic scintillator, specifically liquid organic scintillators and lithium-6 glass.

1.2.1 Liquid organic scintillators

Liquid organic scintillators are organic compounds that produce optical photons when an individual molecule transitions between energy states. The de-excitation decay time is on the order of nanoseconds, and therefore is referred to as prompt fluorescence [1]. Neutrons trigger fluorescence through collisions with large hydrocarbons within the liquid. These collisions reduce the energy of the neutron, thereby slowing them. The lost energy excites the molecules, resulting in prompt fluorescence. Depending on the energy of the neutron, many scintillation events may occur through multiple collisions. However, the neutrons typically lose their energy very quickly, as the similar proton and neutron mass may lead to efficient momentum transfer from the neutron to the protons in the material.

In this work we use mineral oil based scintillators, Eljen EJ-325a and Eljen EJ-325UV. This class of liquid organic scintillators is much safer to use than other liquid scintillators due to its lower flash point [3].

1.2.2 Lithium-6 glass scintillators

Lithium-6 glass distinguishes itself as a neutron detection material due to a relatively large neutron cross section [1]. We used Applied Scintillation Technologies GS20 lithium-6 glass, which is 18% lithium oxide by weight, and 95% of the lithium is lithium-6 [4]. Scintillation occurs through neutron capture, represented in the following reaction [5]



The lithium-6 glass contains cerium ions that affect the energy band structure of the crystal lattice, creating an energy band in the forbidden region that allows electrons to de-excite more quickly [1]. The charged α particle interacts with electrons within these bands, subsequently releasing a

photon as they transition between energy bands [6]. Thus the scintillation process in the lithium-6, cerium doped glass is similar to that of the organic scintillators.

1.2.3 Comparing liquid organic and lithium-6 glass scintillators

There are important differences that characterize liquid organic and lithium-6 glass scintillators. Liquid organic scintillators have a higher light output than lithium-6 glass [3, 4], resulting in lower amplification settings when using the liquid organic scintillator. This causes difficulty when using both simultaneously with the same PMT, as amplifier settings set for the liquid scintillator do not provide sufficient amplification for lithium glass signals. When using such a setup, care must be taken to insure both signals are recorded, as both contain important information regarding the interaction.

As mentioned previously, the liquid organic scintillator also is a moderator for the neutrons, or a material that reduces neutron energies through collisions. Slowing the neutrons increases the number of neutron interactions, as higher energy neutrons without moderation need to be slowed before they can be captured [7]. When used in conjunction with lithium-6 glass, liquid organic scintillators increase the number of neutron captures in the glass while simultaneously providing information on the neutrons through its own scintillation process. This additional information can be used to explore neutrons that interact with only the liquid scintillator and to explore neutrons that interact with both scintillators.

Another important difference lies in the tails of the pulses recorded from both scintillators. The prompt fluorescence in the liquid scintillator occurs more quickly than the transitions initiated by the passing α particles in the lithium-6 glass, while both processes occur more slowly than processes involving gamma excitation. This characteristic distinguishes pulses originating from gamma and neutron interactions, as well as pulses from neutron interactions in the liquid scintillator from those in the lithium-6 glass. The fast processes produce shorter tails than the slow

processes, causing the tails from the liquid scintillator neutron interaction pulses to be shorter than those of the lithium-6 neutron interactions. Gamma ray interactions produce the shortest tails due to the short time interval for the decays in the scintillators.

1.3 Pulse shape discrimination

The tail shapes of gamma pulses and neutron pulses allow the use of pulse shape discrimination (PSD) techniques. Pulse shape discrimination utilizes the different tail lengths and shapes to define parameters that can be used to mathematically distinguish between the several pulse types. There are many different PSD methods; the two most common are the zero crossing method and the charge comparison method [8]. The charge comparison method, which is used in this work, utilizes the integral of the pulse as one parameter used in PSD, as the longer neutron tails produce greater areas (relative to the pulses of equal height) than the shorter gamma tails. However, this single parameter is incapable of distinguishing neutrons from high-energy gammas. The pulses generated by these interactions have longer tails, causing pulse characteristics to be similar to those of neutron interactions. To overcome this limitation, we use multiple other parameters to distinguish the pulses. The pulse area can be split into “early” and “late” areas, and the fraction of early area versus total area is computed. Plotting fraction early versus total area often reveals regions unique to neutron pulses and gamma pulses.

In order to know which regions in the plots of fraction early versus total area are indicative of neutron interactions with a specific material, data must be obtained using different radioactive sources. Californium-252 decays, in part, by spontaneous fission that produces an average of 3.77 neutrons per fission [9]. Therefore, it may be used as a neutron source. Cobalt-60 undergoes β^- decay, resulting in nickel-60 [10]. The ^{60}Ni releases two gamma photons with energies 1.17 and 1.33 MeV [10], and thus ^{60}Co serves as a gamma source. By using these or other sources, the

neutron and gamma regions are determined by comparing the data taken from each source. The regions where ^{60}Co data is most dense will largely be pulses due to gamma rays and the regions unique to the neutron source will largely be pulses from neutrons. There are also regions within the neutron region that indicate where the neutron originated, which can be identified by using the liquid scintillator and the lithium-6 glass separately. Fig. 1.1 shows data taken using ^{252}Cf and ^{60}Co . The region unique to the ^{252}Cf is evident, indicating that pulses in that region were likely generated by a neutron interaction. The ellipse marks the overlap region where it is unknown if a pulse is from a low-energy neutron or a high-energy gamma. The elliptical region between about 0.4 and 0.6 on the fraction early axis indicates neutrons from the lithium-6 glass, while the blue region to the left of the yellow ellipse indicates neutrons from the liquid organic scintillator. These regions are known through comparison of data taken using the scintillators separately (see Fig. 1.2). For a description of the algorithm used to calculate the parameters for PSD, see Sec. 2.2.1.

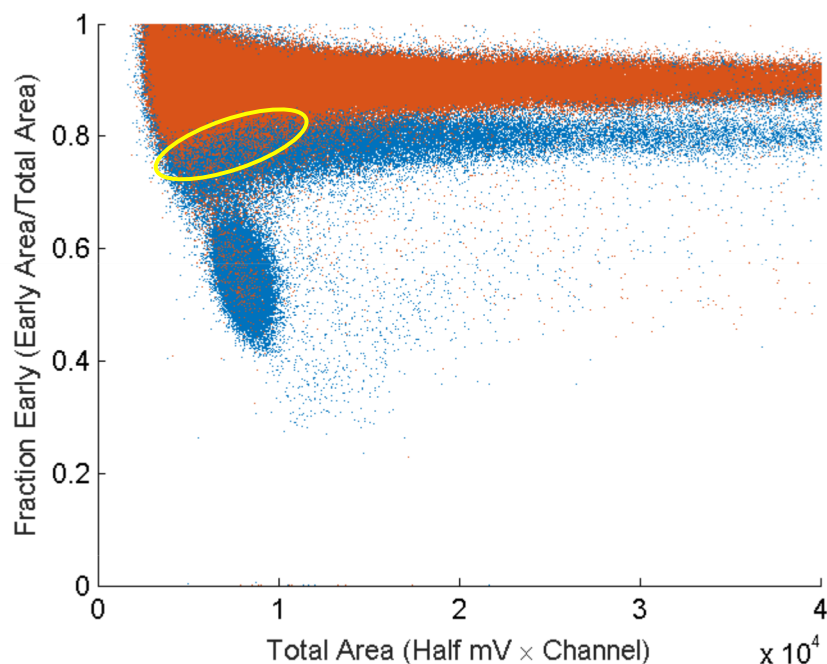


Figure 1.1 Data from ^{60}Co (orange) and ^{252}Cf (blue). The ellipse (yellow) marks where the cobalt gammas overlap the liquid scintillator neutrons.

1.4 Previous and current work

1.4.1 Cadmium capture-gated neutron detector

Previously, the BYU Nuclear Physics Group developed a detector that uses four PMTs with plastic scintillator and cadmium sheets. The plastic serves as a moderator so the neutrons can undergo capture in the cadmium. The purpose of this detector is to detect low-energy neutrons through analysis of the cadmium capture pulses. The detector was calibrated at the Edwards Accelerator Lab at Ohio University, providing excellent energy-dependent response functions. This detector identified neutrons by acquiring a proton recoil pulse from the plastic scintillator followed by a cadmium capture pulse. Identifying neutron using this method allows for good neutron and gamma discrimination [11].

1.4.2 Dual PMT lithium-cadmium neutron detector

Another similar project at BYU involved a dual PMT design utilizing both lithium-6 glass and cadmium. Trevor Jex found that the PMT with the cadmium collected the majority of the counts and behaved similarly to runs using only one PMT and cadmium as a detector. When used together, they had hoped to be able to identify neutrons by looking for a pulse in the cadmium followed by a pulse in the lithium glass, but less than 0.1% of all recorded pulse pairs met the requirements [6].

1.4.3 Hybrid liquid organic scintillator and lithium-6 glass detector: single-pulse analysis

These detectors functioned using similar principles to the detector addressed in this work, which is also discussed by Hill [12]. Capture pulses from the lithium-6 glass are used to identify low-energy neutrons that could not be identified from the liquid scintillator alone, as these neutrons fall in the

gamma-neutron overlap region. We designed a hybrid detector utilizing liquid organic scintillator and lithium-6 glass to combine information from both scintillators (see Sec. 2.1.1). Only one PMT is used, which greatly simplifies the design compared to the previously mentioned detectors. Also, the liquid scintillator possesses PSD capabilities, unlike the plastic scintillator. The moderating material therefore produces additional information about the particle's identity.

Prior to this work, we analyzed pulses individually (called single-pulse analysis) in order to characterize the regions obtained from PSD. Fig. 1.2 displays results from EJ-325a only, from lithium-6 glass with a non-scintillating mineral oil moderator, and from the hybrid detector. Comparing the plots, we can see that the region indicated by the solid line corresponds to liquid scintillator neutron pulses and the region indicated with the dashed line corresponds to lithium neutron pulses. Hill created a new PSD parameter called the after-peaking parameter that was found to improve the distinguishing capabilities of the detector through the grass-like nature of the longer neutron tails (see Sec. 2.2.1 for a description of this parameter) [12].

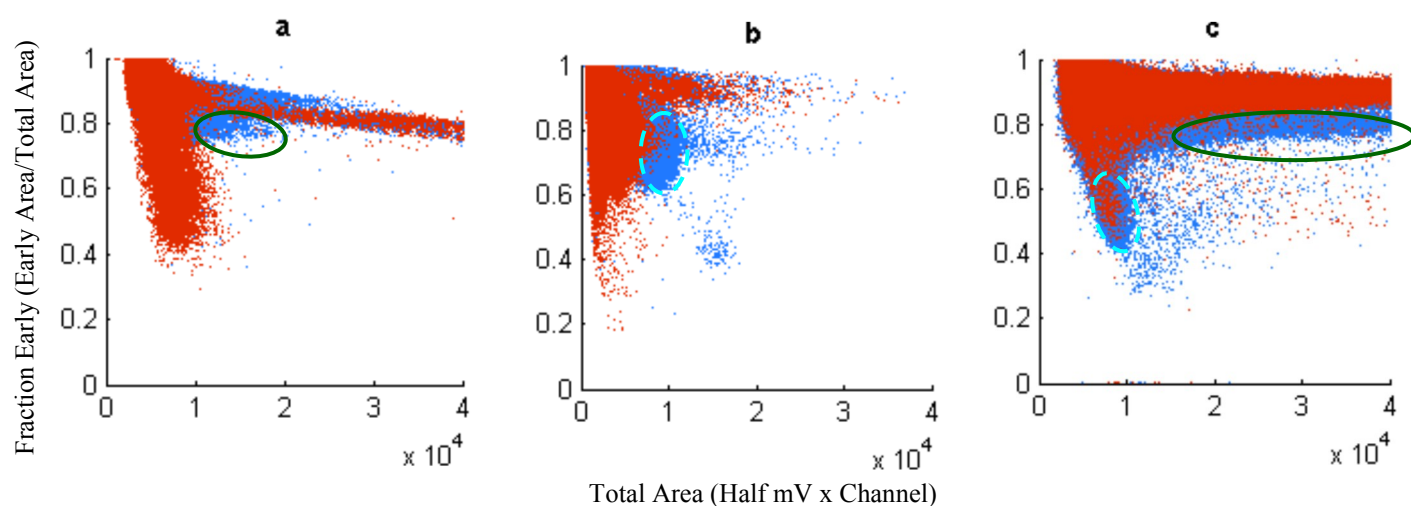


Figure 1.2 Results from (a) EJ-325a alone, (b) lithium-6 glass and mineral oil moderator, (c) hybrid detector, with data from ^{60}Co (red) and ^{252}Cf (blue). The solid line and the dashed line indicate the liquid scintillator and lithium glass neutron regions, respectively. Also, 1 Channel = 4 ns.

1.5 Overview

This work extends previous testing of the capabilities of our hybrid liquid organic scintillator and lithium-6 glass neutron detector, with the goal of improving the detector's pulse shape discrimination (PSD) capabilities. Two mineral oil-based liquid scintillators were used, one with (EJ-325a) and one without (EJ-325UV) wavelength shifting phosphors. The phosphor removal is intended to minimize the significance of lithium glass light absorption in the liquid scintillator (referred to as "self-absorption"). We correlate recoil pulses from the liquids to capture pulses in the lithium by searching for events containing a recoil pulse followed by a capture pulse. Recoil pulses are defined using the regions and the after-peaking parameter defined in previous work (see Fig. 1.2, Hill [12]).

I obtained additional information from the individual pulse analysis by applying principal component analysis (PCA) and feature and Fisher weighting. These methods quantify the separating abilities of various pulse characteristics, but fail to significantly improve PSD.

My role in the project has primarily been to acquire and analyze the data. I have both adapted existing MatLab code and written my own in order to perform the analysis. I have also participated in the design process and the work performed concerning the analysis of individual pulses.

Analysis of the correlated pulses demonstrates a decrease in the ratio of misidentified cobalt-60 and radium gamma rays to total number of counts by a factor of 1000. They are largely independent of which liquid scintillator is used in the detector, though the EJ-325UV detector identifies 20–40% more neutrons from the ^{252}Cf source, indicating that self-absorption may occur in the EJ-325a detector; however, more analysis is needed to determine the statistical significance of the results. The detector design results in reduced neutron efficiencies, indicating that some neutrons may be discarded by the analysis routine.

Chapter 2

Experimental and analytical methods

In this chapter, we will discuss the experimental and analytical methods used in this work. The experimental methods section (Sec. 2.1) describes how data were acquired. Specifically, the detector design, equipment and electrical setup, and radioactive sources are described in Secs. 2.1.1, 2.1.2, and 2.1.3, respectively. The analytical methods section (Sec. 2.2) describes how the data were analyzed. The pulse shape discrimination algorithm, principal component analysis, feature and Fisher weighting, correlated pulse analysis, and efficiency calculations are described in Secs. 2.2.1, 2.2.2, 2.2.3, 2.2.4, and 2.2.5, respectively.

2.1 Experimental methods

2.1.1 Detector design

We designed our detectors using two $15\text{ cm} \times 15\text{ cm} \times 25.2\text{ cm}$ glass containers. The glass sheets composing the containers are 0.5 cm thick; thus the inner dimensions are $14\text{ cm} \times 14\text{ cm} \times 24.7\text{ cm}$. A 5 in (12.7 cm) diameter, 1 mm thick Applied Scintillation Technologies (AST) GS20 lithium-6 glass sheet was placed on the bottom of each container. The GS20 sheet is 18% lithium

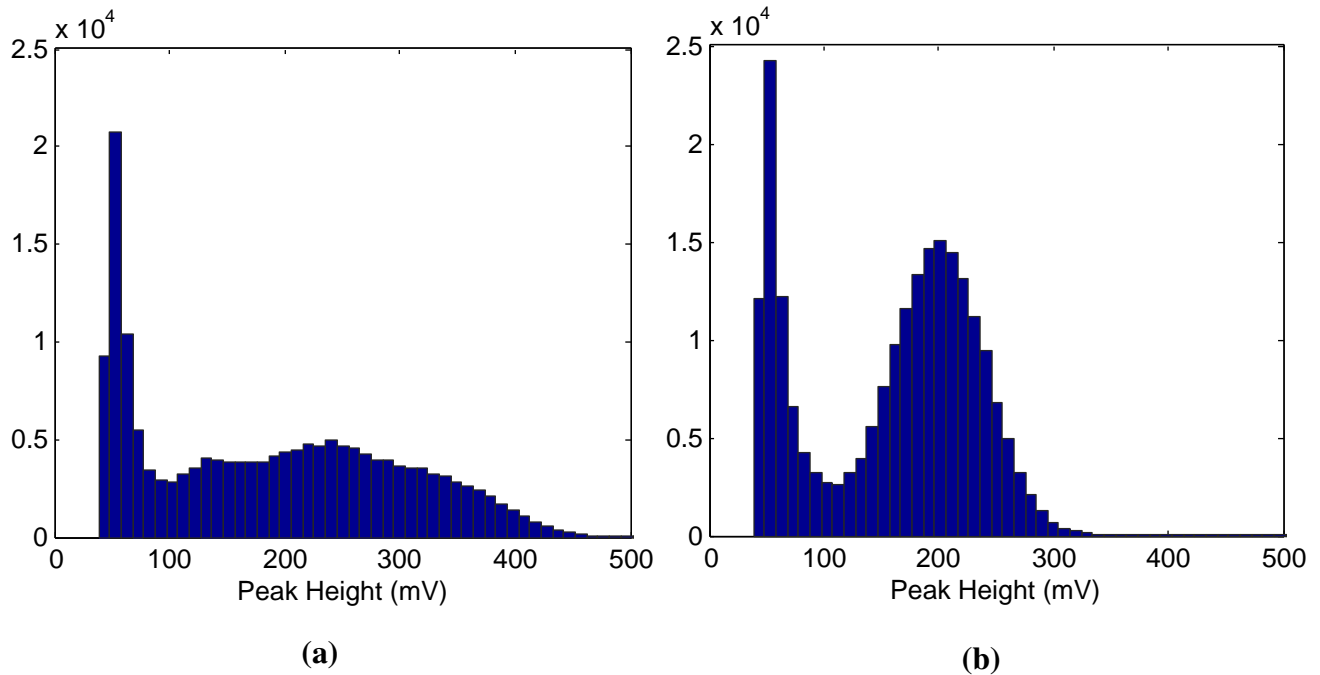


Figure 2.1 Peak distributions using lithium-6 glass and mineral oil depths of 2.5 cm (a) and 4.0 cm (b), respectively. At low depths, the neutron pulse peak height distribution is smeared out, leaving a relatively flat distribution at the higher peak heights. More mineral oil means more moderation, indicating that the distribution becomes more peaked as the higher energy neutrons are moderated.

oxide by weight, and, of the lithium present, 95% is lithium-6 [4]. We used this location because placing the lithium-6 glass closer than 4.0 cm to the PMT face produces a trimodal peak height distribution when used in conjunction with a mineral oil moderator, and we found we obtained better PSD with greater distance from the PMT face to the lithium-6 glass. We expected to see a bimodal distribution, one mode corresponding to the detected gamma rays and the other to the neutrons. This expected distribution appeared when the lithium-6 glass was situated 4.0 cm or greater from the PMT face. Fig. 2.1 shows the peak height distributions observed using GS20 glass and mineral oil at oil depths of 2.5 cm (see Fig. 2.1a) and 4.0 cm (see Fig. 2.1b).

The mineral oil based liquid scintillator was poured on top of the lithium-6 glass. We chose a mineral oil based scintillator for two reasons. First, we expected the scintillator to moderate

the neutrons similarly to the mineral oil used along with the lithium-6 glass in our previous explorations into the behavior of the lithium glass. Second, the Eljen EJ-325 is much safer to use than scintillators such as EJ-301. The flash point of EJ-301 is 26°C [13], while the flash point of EJ-325 is 146°C [3]. Since it is less volatile, EJ-325 may be used in containers that are not sealed, resulting in a simpler detector setup. We used two different types of mineral oil based scintillator: EJ-325a and EJ-325UV. The latter was specially ordered without a wavelength shifting phosphor, causing the output spectrum of the scintillator to shift towards uv light relative to EJ-325a. The presence of the phosphor may cause self-absorption in the detector, as the light emitted from the lithium glass may be absorbed by the liquid scintillator prior to reaching the PMT. Thus we utilized both scintillators in order to determine the importance of self-absorption in our hybrid detector.

The PMT was inserted approximately 2 mm into the liquid scintillator such that the face of the PMT was 6.5 cm from the bottom of the container. Immersing the tube into the liquid insured

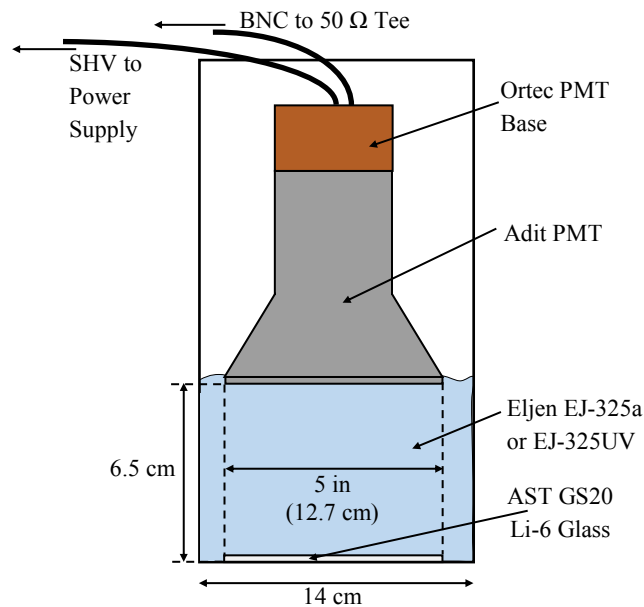


Figure 2.2 A simplified schematic depicting the detector setup. The support system for the PMT is omitted for simplicity. Note two types of scintillators were used, using the same PMT but separate containers.

good optical coupling, increasing the efficiency of light collection by decreasing the number of material interfaces with differing indexes of refraction. The PMT was clamped about the neck to two rubber-tipped rods that were in turn clamped to support system that rested on top of the glass container. This system positioned the PMT face parallel to the lithium-6 glass sheet. Fig. 2.2 depicts the setup, omitting the support system for clarity. There are two detectors, one for each scintillator. Each has a different sheet of GS20 glass, but we acquired all data using the same PMT and PMT base.

After inserting the PMT, we bubbled the liquid organic scintillator with argon. The presence of oxygen in the scintillator can affect its PSD capabilities and light output [14]. The bubbling of argon removes the oxygen from the scintillator, improving light output and PSD. We bubbled argon at a rate of 25–40 mL/min. The rate varied significantly, as the regulator used to determine the flow rate was designed for much larger flow rates. Thus it was difficult to accurately select a flow rate and the rate was not constant through the duration of the bubbling. For the correlated-pulse analysis, data were taken after 6.5 hours of bubbling.

2.1.2 Equipment and setup

We used an Adit B133D01S PMT with an Ortec 266 14 pin PMT base. We powered the PMT using 1200 V provided by an Ortec 556 high voltage power supply. Data were acquired from the anode using a standard BNC connector. We placed our detector in a light tight plywood box in order to protect the PMT from ambient light that would damage it. The box has outer dimensions 75.9 cm \times 76 cm \times 91.2 cm, with wall thicknesses of 1.8 cm. Feedthroughs allowed the safe high voltage (SHV) connector and BNC connectors to be attached to the PMT without compromising the integrity of the box.

The anode signal was then split using a 50 Ω tee, and the two signals were run into two separate Ortec 474 amplifiers. The resistance in the tee reduces ringing in the signal. The split signals are

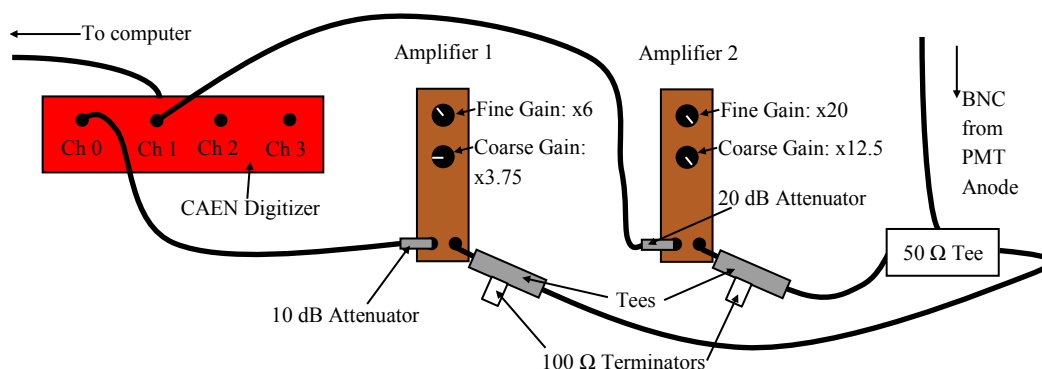


Figure 2.3 Electrical setup for pulse recording. Amplifier 1 has been set to optimize the pulse heights for pulses from the liquid scintillator while amplifier 2 is set to optimize for lithium glass pulses. The difference in settings is due to the higher liquid scintillator light output.

fed into the amplifiers using tees with $100\ \Omega$ terminators on the unused end of the tee, also to reduce ringing. We split the signal this way to account for the difference in light outputs of the lithium and liquid scintillators. The light output of the GS20 glass is 20%–30% the light output of anthracene [4], while EJ-325a has 62% its output [3]. A Costruzioni Apparecchiature Elettroniche Nucleari S.p.A. (CAEN) DT5720 4 channel 12 bit 250 MS/s desktop waveform digitizer was used to convert the analog signal into data files, where in this case channels represents the source of the data, rather than a time analog. However, the CAEN digitizer has a maximum pulse height of 1 V. Consequently, we chose amplifier settings such that the amplified pulses were under 1 V, and to further protect the digitizer, a 10 decibel attenuator was attached to the output of the first amplifier and a 20 decibel attenuator was attached to the second. We set the first amplifier to optimize the peak heights of pulses from the liquid scintillator and the other to do the same for the lithium-6 glass pulses (See Fig. 2.3 for the gain settings on the amplifiers and the schematic of the electrical setup). Thus the pulses from the lithium glass appeared insignificant in the signal from the first amplifier, and the liquid scintillator pulses seemed extremely large in the second signal.

We obtained information from both the lithium glass and the liquid scintillator by recording

each signal on separate channels and then digitally recombining them. Data are recorded by interfacing with the CAEN, which is controlled by a program called BEST CONTROLLER that was designed specifically for the BYU nuclear physics group. This program digitally triggers the CAEN to record pulses only when above a certain threshold. We set the CAEN to trigger when a pulse from the second signal was below -100.1 mV (the anode voltages are negative). The CAEN then records the pulse from both signals. When analyzing single pulses, we set the digitizer to record approximately 400 ns prior to the trigger and 1.648 μ s after the trigger, resulting in a time window of approximately 2 μ s. An event is defined by each digitizer trigger, and each event includes one or more pulses. When seeking for correlated pulses, an event is 32 μ s long, where half of the time window is the signal prior to the trigger and half after the trigger.

2.1.3 Radioactive sources

Radioactive sources provided the neutrons and gammas needed to test our detector. We used ^{252}Cf as a neutron source. This isotope of californium has a half-life of 2.645 years and 96.908% of all decays are α decays, with spontaneous fission accounting for the remaining 3.092% [15]. Each fission results in an average of 3.77 neutrons per fission [9], making ^{252}Cf an ideal choice for a neutron source. The californium was placed on the floor 38.6 cm away from the bottom of the

Table 2.1 Information regarding the radioactive sources used in the experiment. Radium is omitted, as the sources used are not calibrated and the decay paths of radium are numerous, leaving some doubt as to what products remain. See Martin [15] and Browne [10] for information regarding ^{252}Cf and ^{60}Co , respectively. Also note that the other 3.092% of ^{252}Cf decays are spontaneous fission, which emit on average 3.77 neutrons per fission [9].

Source	Reference Date	Activity Rate (kBq)	$\tau_{1/2}$ (yrs)	Decay Scheme
^{252}Cf	1 Aug 2012	3292	2.645	α (96.908%)
^{60}Co	1 Aug 2010	346.1	5.271	β^- (100%)

plywood box.

For gamma sources, we utilized ^{60}Co and radium. The cobalt produces two gamma photons with energies 1.17 MeV and 1.33 MeV, respectively [10]. The radium has many decay paths, and thus produces a range of gamma energies, some of which are higher energies than those produced by the decay of ^{60}Co . Thus both sources are used in order to compare the response of the detector to a variety of gamma energies. Both of these sources were placed 20.5 cm off the floor (18.1 cm from the bottom of the box) on top of a stack of paraffin blocks. We placed the sources at these distances to obtain comparable count rates for all three sources. The activity rates, the dates they were determined, half-life, and decay schemes for the ^{252}Cf and ^{60}Co sources are included in Table 2.1.

2.2 Analytical methods

2.2.1 Pulse shape discrimination

In addition to the pulse area, our PSD algorithm defines several other parameters for use in comparison. These parameters are peak height (P_H), total area (A_T), width (W), early area (A_E), late area (A_L), the fraction of early area to total area (F_E), the centroid of the peak (P_C), and the number of times the pulse exceeded 5% of the maximum peak height, called the after-peaking parameter (A_P). Table 2.2 presents the parameters and a summary definition for each. The demarcation between early and late areas, as well as the beginning and ending of the pulse are defined by the early, late, and early/late lines. For single-pulse analysis, the algorithm begins by locating the maximum, thereby determining the peak height and the location of the centroid. The early, late, and early/late lines are then defined using user-defined offsets. We defined the early line to be ten channels prior to the channel at which the rising edge reached 30% of the maximum, where one channel is four nanoseconds. The late line is defined similarly, being offset 300 channels

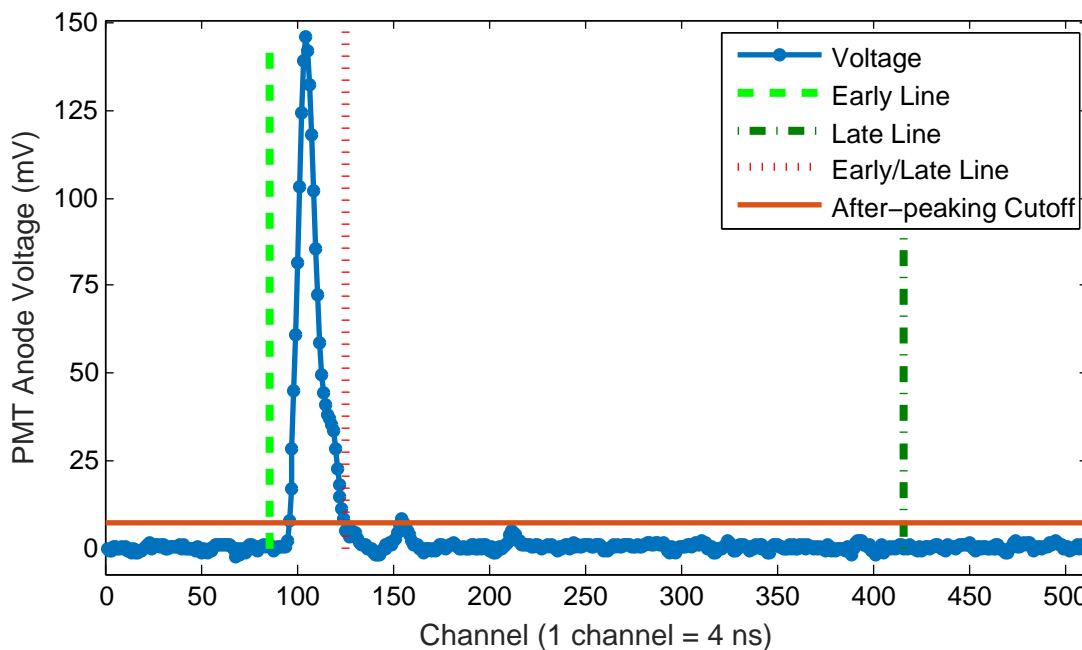


Figure 2.4 This event demonstrates the placement of the early, late, and early/late lines, as well as the after-peaking cutoff. The early/late line is placed as to emphasize the increased late area for neutron events.

later in time from the point where the falling edge is 30% of the maximum. These two lines mark the beginning and end of the pulse. The early/late line is set 40 channels from the early line, and it marks the end of the early area and the beginning of the late area. We chose these values to define the pulses because trial and error demonstrated these values to produce the best separation when the fraction of early area to total area was plotted against the total area. Fig. 2.4 plots a gamma event with its corresponding early, late, early/late, and after-peaking cutoff lines. The early/late and late lines have been placed relatively late in the peak compared to the centroid in order to emphasize the effects the long tails of neutron events have on the parameters. Because of this choice, the neutron event fraction early parameter is lower than that of gamma events, giving the best separation as mentioned previously.

To calculate the total, early, and late areas, we sum the signal between the early and late lines,

Table 2.2 Parameters used for PSD, their descriptions, and units. The Early line is defined as ten channels earlier in time than the channel at which the rising edge reaches 30% of the maximum and marks the beginning of the pulse. The Early/Late line is defined as 40 channels later in time than the Early line and marks the division between Early and Late area. The Late line is defined as 300 channels later in time than the channel at which the falling edge reaches 30% of the maximum and marks the end of the pulse.

Symbol	Description	Units
P_H	Maximum voltage of the pulse	mV
A_T	Total area under the curve	mV \times channel (1 channel = 4 ns)
W	Difference between Late and Early lines	channel
A_E	Area between Early and Early/Late lines	mV \times channel
A_L	Area between Early/Late and Late lines	mV \times channel
F_E	Ratio of Early and Total Areas	Dimensionless
P_C	Channel number of the pulse center	channel
A_P	Count tail peaks exceeding 5% the maximum	Dimensionless

the early and early/late lines, and the early/late and late lines, respectively, thus approximating the integral with a Riemann sum. The width is calculated using the difference in position of the early and late lines, and the fraction early is the ratio of early area to total area. The only parameter left to calculate is the after-peaking parameter. This parameter is the number of times the signal crosses a line defined as 5% the pulse maximum. The line representing the cutoff is shown in Fig. 2.4. As described in Chapter 1, when a neutron interacts with either the liquid scintillator or the lithium-6 glass, the resulting pulse decays more slowly. This produces a longer tail than a gamma ray interaction. The tail resembles many smaller peaks that are larger than background noise. Lithium-6 neutron pulses contain more of these peaks than pulses originating from the liquid scintillator, so the after-peaking parameter improves our ability to distinguish not only between pulses produced by gammas and neutrons, but also neutron pulses produced in the liquid scintillator and the lithium

glass.

After calculating the parameters, we plot the parameters as either histograms or scatter plots. Peak height, total area, and width are plotted as histograms, as typified by the distributions shown in Fig. 2.1. For single-pulse analysis, the plots fraction early versus total area, early versus late area, and peak versus total area showed clear regions representing gammas, neutrons from the liquid scintillator, and neutrons from the lithium glass. We principally use the fraction early versus total area plot to effect the correlated-pulse analysis, as the regions are most easily distinguishable using these parameters. This will be explained in detail in Sec. 2.2.4.

2.2.2 Principal component analysis

Attempting to improve our PSD, I applied principal component analysis (PCA) to the single-pulse data acquired. I hoped that this statistical analysis method would improve upon the visual separation by finding the axes in the data that point in the direction of maximum variance, thereby emphasizing the variance in the data [16].

The first step of PCA is to autoscale the data. Autoscaling refers to the process of removing weighting caused solely by the units while remaining relatively insensitive to outliers. Dimensionless parameters are introduced, defined as

$$x'_{ik} = \frac{x_{ik} - \bar{x}_k}{s_k}, \quad (2.1)$$

where x'_{ik} is the k^{th} dimensionless parameter of the i^{th} pulse, and s_k is the standard deviation of the k^{th} parameter. This is defined as

$$s_k = \left[\frac{1}{N-1} \sum_{i=1}^N (x_{ik} - \bar{x}_k)^2 \right]^{1/2}, \quad (2.2)$$

where N is the total number of events. Autoscaling all of the parameters gives the variance of each dimensionless parameter to be 1.0 [16].

After autoscaling the data, the data matrix is constructed by filling the columns with the autoscaled parameters (other than the centroid) such that each row of the matrix represents a single pulse. We will define this matrix to be \mathbf{X} . The columns correspond to the following scaled parameters: total area, fraction early, peak height, width, late area, early area, and the after-peaking parameter. We now define the correlation matrix, \mathbf{C} , as

$$\mathbf{C} = \frac{1}{N_k - 1} (\mathbf{X}^T \mathbf{X}), \quad (2.3)$$

where N_k represents the total number of parameters in \mathbf{X} [16].

The correlation matrix is important, as its eigenvectors form the principal axes of the data. The eigenvector that corresponds to the largest eigenvalue points in the direction of greatest variance, the eigenvector that points to the second largest eigenvalue points in the direction of second greatest variance, and so forth. The overall contribution to the variance can be determined by the ratio of the eigenvalue to the sum of all the eigenvalues. The elements of the vectors are referred to as loadings, and the size of the element determines the contribution of the corresponding parameter to the variance [16].

For example, if the largest component of the first eigenvector is the first element, total area contributes the greatest to the variance. If it were the second, then fraction early would contribute the greatest, and so forth, corresponding to the order the parameters were placed in the correlation matrix. This allows for a quantifiable measure of which parameters are most important in separating neutron and gamma events when performing PSD.

To visualize the principal axes, we define the matrix \mathbf{Y} as

$$\mathbf{Y} = \mathbf{X}\mathbf{R}, \quad (2.4)$$

where \mathbf{R} is a rotation matrix formed using the eigenvectors of \mathbf{C} as its columns [16]. Each column of \mathbf{Y} then represents the data rotated onto the corresponding principal axes. In most cases, the majority of the variance is contained in the first two eigenvectors, so only principal axes 1 and 2

are compared.

2.2.3 Feature and Fisher weighting

One limitation of PCA is that it takes into account the variance due to all events. This may result in less significant results when analyzing our data, as a large number of events will be gamma events, thereby reducing the variance. It does not allow for analysis of the variance between specific regions, as it treats each event separately. Feature and Fisher weighting, however, specifically compare the variances of the regions. Each type of weighting calculates a specific weight for each of the parameters of interest [16].

Feature weighting utilizes a ratio of intercategory variances to the sum of intracategory variances, where category is synonymous with region, to produce a variance weight for each parameter (i.e. feature), with one weight per pair of categories. In other words, a variance weight is calculated by comparing the parameters of each pair of regions to one another, thereby producing one variance weight per parameter per pair. The expression for the variance weights is

$$w_k(\text{I}, \text{II}) = 2 \times \frac{(1/N_{\text{I}}) \sum x_{\text{I}}^2 + (1/N_{\text{II}}) \sum x_{\text{II}}^2 - (2/N_{\text{I}}N_{\text{II}}) \sum x_{\text{I}} \sum x_{\text{II}}}{(1/N_{\text{I}}) \sum (x_{\text{I}} - \bar{x}_{\text{I}})^2 + (1/N_{\text{II}}) \sum (x_{\text{II}} - \bar{x}_{\text{II}})^2}, \quad (2.5)$$

where k represents the parameter index, x represents the parameter value for a given pulse, N represents the total number of pulses in the region, I represents the first category or region and II represents the second. The numerator represents the intercategory variance and the two terms in the denominator represent the intracategory variances. Note that each sum is over all pulses in the selected region [16].

The total weight for each feature is the product of all the variance weights for each parameter. This weight is also known as the feature's overall discriminating ability, and it is calculated using the following formula

$$w_k = \left[\prod_{j=1}^{N_j} w_k(j) \right]^{1/N_j}, \quad (2.6)$$

with j representing each pair and N_j being the total number of pairs. Each weight will be greater than or equal to one. If the weight is larger, that feature contributes more to the variance between the regions [16].

Fisher weighting is similar to feature weighting, but the variance weights are calculated as the ratio of the absolute value of the difference of the category means to the intracategory variances. Thus, the variance weight is

$$w_k(\text{I}, \text{II}) = \frac{|\bar{x}_\text{I} - \bar{x}_\text{II}|}{(1/N_\text{I})\sum(x_\text{I} - \bar{x}_\text{I})^2 + (1/N_\text{II})\sum(x_\text{II} - \bar{x}_\text{II})^2}, \quad (2.7)$$

with I, II, N , k , and x using the same definitions as in Eq. 2.5. Also, the Fisher weight for each parameter is not the product of the variance weights, but rather

$$w_k = \frac{1}{N_j} \sum_{j=1}^{N_j} w_k(j), \quad (2.8)$$

again using the same definitions as Eq. 2.6. These weights, in contrast to feature weights, may be equal to zero [16].

Either method may be used in order to determine which parameters best separate two distinct regions, and they provide additional insight into which parameters best separate neutrons and gammas. The PCA values are skewed by the large number of gamma events and are, in reality, only demonstrating which parameters contribute to the overall variance.

2.2.4 Correlated pulses

The main goal of this work, however, was to extend the single pulse analysis into correlated-pulse analysis. Correlated-pulse refers to two pulses that correspond to a liquid neutron pulse followed by a lithium glass neutron pulse. We expect neutrons to interact first with the liquid scintillator, as the liquid scintillator moderates the neutrons, and then be captured by the lithium-6. We looked for pulses that are within 16 μs of one another, as any larger time gap leaves a large possibility for

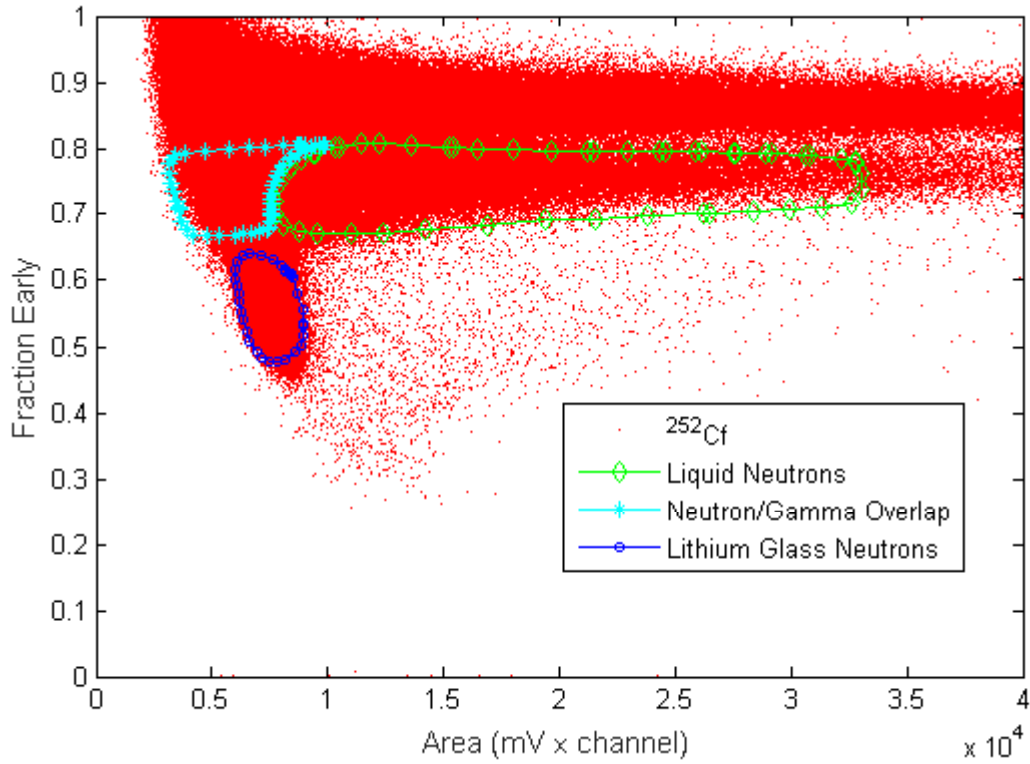


Figure 2.5 The regions used as references in the correlated-pulse analysis. Note that the regions do not seem distinct due to the scaling. See Fig.2.6 for an inset of this plot.

two pulses to be correlated when the pulses actually came from two different neutrons. To look for these pulses, we extended the time acquisition window to $32 \mu\text{s}$, roughly $16 \mu\text{s}$ before and after the trigger to allow for triggering off of either the liquid neutron pulse or the lithium neutron pulse.

Using regions we discovered in single-pulse analysis, we were able to analyze each pulse in each event separately in order to individually characterize each pulse. Each dataset included a reference run that was obtained using a ²⁵²Cf source with the acquisition window set for single-pulse analysis as described in Sec. 2.1.2. The regions were then selected by drawing the region in MatLab and passing the region to the analysis algorithm. Fig. 2.5 displays the reference regions used in our analysis, and Fig. 2.6 is a close-up view of the same reference, in order to emphasize our choice of the lithium glass neutron region.

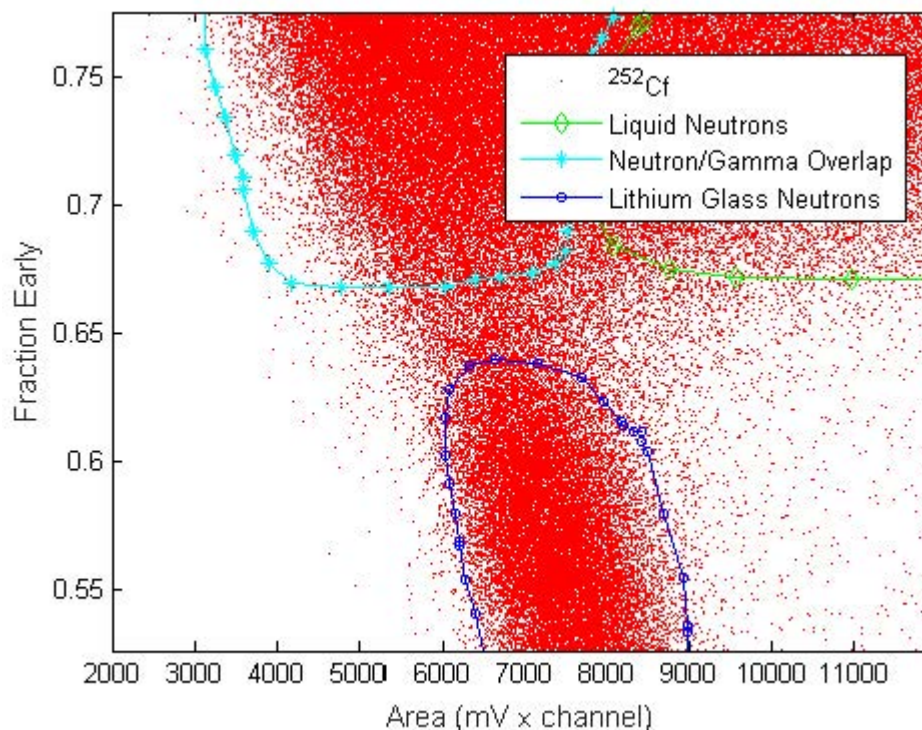


Figure 2.6 An inset of Fig. 2.5. The density of events in the lithium neutron region is much higher than that of the region in between the three reference regions, indicating a separate region.

There are two different algorithms used. After finding an event with multiple pulses, the first algorithm checks the first pulse against the liquid neutron region. It also checks that the peak is taller than the following peak (as the liquid scintillator has a higher light output), and it checks if the after-peaking parameter is between 4 and 8. Hill determined that events in the liquid neutron region fell into that range, while the lithium neutron events had after-peaking parameters of 10 or greater [12]. Fig. 2.7 shows the fraction early versus total area plot with pulses limited by the after-peaking parameter. Fig. 2.7(a) only plots pulses with $A_P < 4$, Fig. 2.7(b) plots pulses with $4 \leq A_P \leq 8$, and Fig. 2.7(c) plots pulses with $A_P \geq 10$. The shift towards the liquid neutron region and then the lithium neutron region; however, the regions are not completely isolated, indicating some overlap in the after-peaking regions used. The effectiveness of the after-peaking parameter

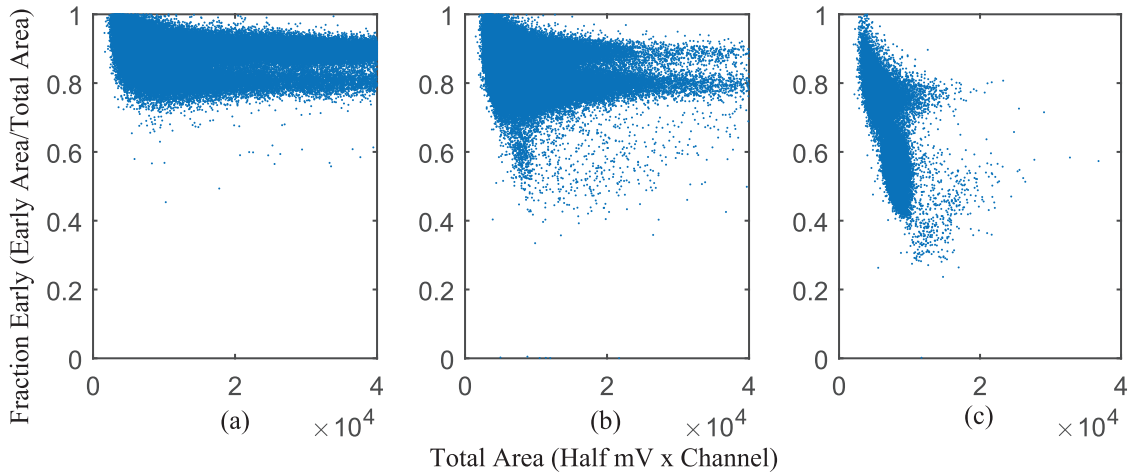


Figure 2.7 Fraction early versus total area for ^{252}Cf , with A_P (a) less than 4, (b) between 4 and 8, and (c) greater than 10. In (a), we can see that the majority of the pulses are in the upper gamma region, with some in the liquid neutron region. In (b), we can see that the pulses have shifted into the liquid neutron region, though some are still in the gamma region. In (c), we can see a significant number of pulses in the lithium neutron region. This illustrates how A_P helps narrow the classification of neutrons, but still is used in conjunction with the other parameters.

lies in being used in conjunction with the fraction early versus total area regions, and together they serve to improve PSD. It should be noted that being more selective helps increase separation, but decreases efficiency. In this work, a balance between increased PSD and good efficiency was chosen by using the above parameters.

If the first pulse falls into the after-peaking range mentioned previously, it has passed all the tests and the second pulse is then checked against the lithium neutron region and the after-peaking parameter. Once all checks are passed, the event is confirmed as a neutron.

The second algorithm proceeds in the reverse order. The second pulse is checked against the lithium region and the after-peaking parameter, and if it passes, the first pulse is checked against the liquid region. In this case, however, it is not required that the liquid pulse be taller than the lithium peak. We check the lithium pulse first because that region does not overlap significantly with the gamma region (see Fig. 2.5). If we know the second pulse is a lithium neutron event,

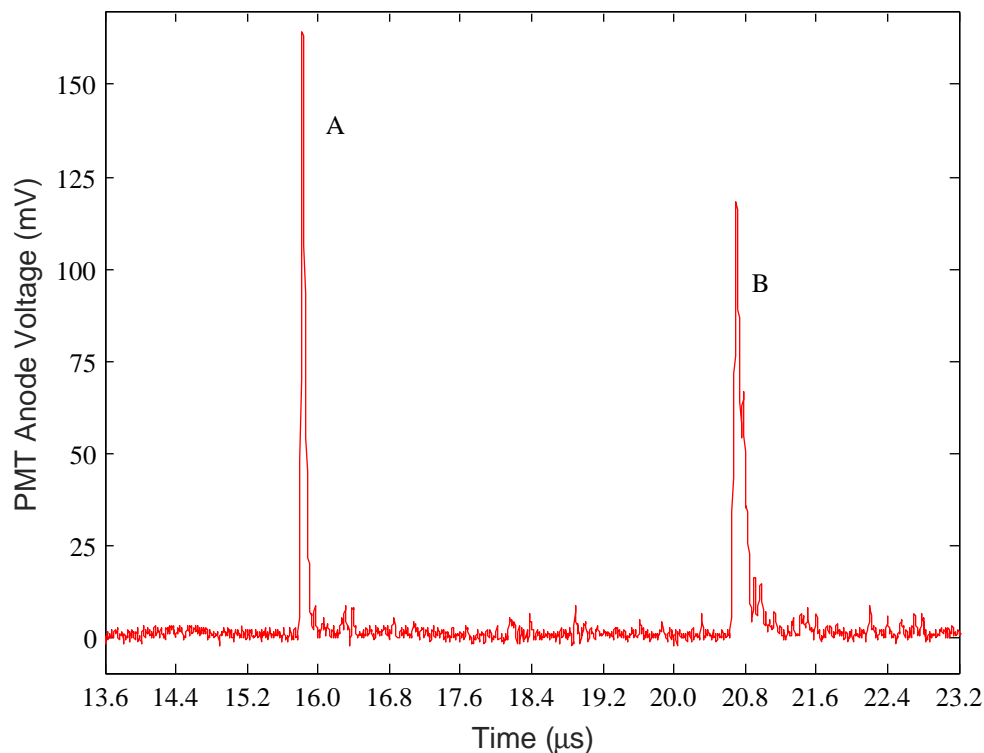


Figure 2.8 This event represents a neutron that first interacted with the liquid scintillator and subsequently was captured in the lithium-6 glass. The peak labeled A is due to the neutron's interaction in the liquid and the peak labeled B is a result of the capture in the glass. The voltages recorded from the PMT anode have been shifted so the average background is 0 mV. Time is measured from the beginning of each event, but only the portion of interest is shown.

than if the first falls in either the overlap region or the known liquid scintillator neutron region, we know that the event is a neutron. This allows us to find neutrons in the overlap region, where low-energy neutrons mingle with the higher-energy gammas. Thus we do not constrain the peak height on the first pulse in order to allow for the lower range of energies to be included in our results. Fig. 2.8 shows an example of an event with correlated pulses. The first pulse has a tail with some after-peaking, more than that which is found in gamma events, while the second has the significant after-peaking characteristic of lithium glass neutron events.

2.2.5 Efficiency calculations

In order to quantify our detector's performance, specifically the detector's ability to detect neutrons, I calculated the detector efficiency. In this work, there are two different efficiencies; the first is relative efficiency, which is the ratio of events classified as neutrons to the total number of events. The second is absolute efficiency. Absolute efficiency is the ratio of neutron events to the theoretical number of neutrons that passed through the detector in the duration of the data acquisition period.

To calculate the theoretical number of neutrons, we first must calculate the solid angle (Ω) of the detector. The solid angle is the analog of an angle, but in three dimensions, with units of steradians. An angle is defined as the ratio of arc length to radius (or distance from the origin); a simplified definition of solid angle is the ratio of an area to the distance squared from the origin, but this is technically only true for the inner surface of sphere that is centered at the origin. The solid angle for other shapes is more difficult to compute; in this work, a Monte Carlo integration method was used. When calculating efficiency, we assume an isotropic point source. Thus once the total number of particles emitted from the source is calculated, we need only multiply that number by the ratio of the solid angle to the solid angle of a sphere (which is 4π steradians) to determine the number of counts that passed through the detector.

The next step is to determine the number of particles emitted by the source. We first determine the activity of the source in becquerel (Bq) using the rate equation for radioactive decay [1], which gives

$$R = R_0 e^{-\ln(2)t/\tau_{1/2}}, \quad (2.9)$$

where R is the activity, R_0 is the initial activity, t is the elapsed time and $\tau_{1/2}$ is the half-life of the material. The elapsed time was calculated from the date the source was calibrated, which is found in Table. 2.1. Once the activity is calculated, the total number of emitted particles is calculated by simply multiplying by the duration of the data acquisition period, except for specific circumstances.

The principal exception is for cases in which the source decays through multiple paths. This is true of ^{252}Cf , for which 96.908% of all decays are α decays and the other 3.092% are fission events [15]. We are most concerned with the fission decays, as these produce the neutrons that we detect. The half-life of ^{252}Cf includes all decays, not just fission events. Thus, once we have the activity, we must also multiply by the factor 0.03092 to take into account that percentage of fission decays. Furthermore, each fission produces on average 3.77 neutrons [9], indicating that we must multiply by that factor as well in order to obtain the actual number of neutrons emitted during the data acquisition. Therefore,

$$N_{theory} = 0.03092 \times 3.77 \times R \times t \times \frac{\Omega}{4\pi} \quad (2.10)$$

for ^{252}Cf , and for ^{60}Co the factors 0.03092 and 3.77 would be removed. The value N_{theory} is the theoretical number of neutrons (or gammas) that passed through the detector. Note that t indicates the duration of data acquisition, rather than time elapsed from the calibration of the source as in Eq. 2.9. Once N_{theory} is calculated, the absolute efficiency is calculated as the ratio of the events classified as neutrons to N_{theory} .

In this work, the term efficiency refers to the value of ϵ_{abs} calculated when using the ^{252}Cf source. When the ^{60}Co or Ra sources are used, the ratio will instead be known as the misidentified gamma ratio, as the events classified as neutrons came from a gamma source, thus classifying gammas as neutrons.

Chapter 3

Results

In this chapter, I will present the results of my data analysis. Sec. 3.1 presents the statistical analysis applied to data analyzed using single-pulse analysis, with Sec. 3.1.1 describing the results of the principal component analysis and Sec. 3.1.2 presenting the feature and Fisher weighting analysis. The correlated-pulse analysis results are then described in Sec. 3.2. The significance of the results is presented in Sec. 3.3, and the conclusions are summarized in Sec. 3.4. Finally, Sec. 3.5 describes possible considerations for further work.

3.1 Statistical analysis

3.1.1 Principal component analysis

Principal component analysis was performed upon data initially analyzed using the single pulse analysis method. Table 3.1 contains the eigenvalues (see Table 3.1a) and eigenvectors (see Table 3.1b) of the correlation matrix. Computing the ratio of the sum of the first three eigenvalues to the total sum of the eigenvalues demonstrates that the first three eigenvectors contain approximately 91% of the variance in the data. The ratios of individual eigenvalues are also found in Table 3.1a.

Table 3.1 Eigenvalues (λ_i) and Eigenvectors (ξ_i) from principal component analysis of data acquired using EJ-325UV and ^{252}Cf . The second row of the λ_i table lists the fraction of the total variance contained within the corresponding ξ_i . Within each ξ_i , the loading with the largest values correspond to the parameters in the first column with the greatest effect on the variance.

(a) Eigenvalues							
	λ_1	λ_2	λ_3	λ_4	λ_5	λ_6	λ_7
λ_i	1.85×10^5	1.01×10^5	3.53×10^4	1.99×10^4	1.02×10^4	4.45×10^2	1.21
$\lambda_i / \sum_{i=1}^N \lambda_i$	0.526	0.287	0.100	0.0566	0.0290	1.27×10^{-3}	3.43×10^{-6}

(b) Eigenvectors							
Loadings	ξ_1	ξ_2	ξ_3	ξ_4	ξ_5	ξ_6	ξ_7
A_T	-0.520	0.0364	6.20×10^{-3}	-0.0109	0.0910	0.397	0.749
F_E	-0.0362	-0.488	0.840	-0.228	-0.0584	-8.49×10^{-3}	-1.29×10^{-4}
P_H	-0.510	-0.0516	-0.0231	0.0312	0.403	-0.758	3.77×10^{-3}
W	0.0179	0.0570	0.510	0.644	0.0280	-0.0250	-1.10×10^{-4}
A_L	-0.426	0.299	0.031	-0.249	-0.788	-0.165	-0.131
A_E	-0.517	-0.0186	5.17×10^{-4}	0.0377	0.266	0.489	-0.649
A_P	0.141	0.586	0.186	-0.684	0.365	0.0253	4.38×10^{-5}

The first eigenvector's largest loadings correspond to the total pulse area, peak height, early area and late area, while the second vector's principal loading corresponds to the after-peaking parameter, the fraction of early area to the total area, and the late area. Therefore, the total area, peak height, early area, late area, after-peaking, and fraction early parameters are the primary factors in distinguishing pulse regions. Fig. 3.1a plots fraction early versus total area, Fig. 3.1c plots peak height versus total area, and Fig. 3.1e plots late area versus early area, while Figs. 3.1b, 3.1d, and 3.1f contains insets of the same plots. We can see distinct regions representing recoil pulses due

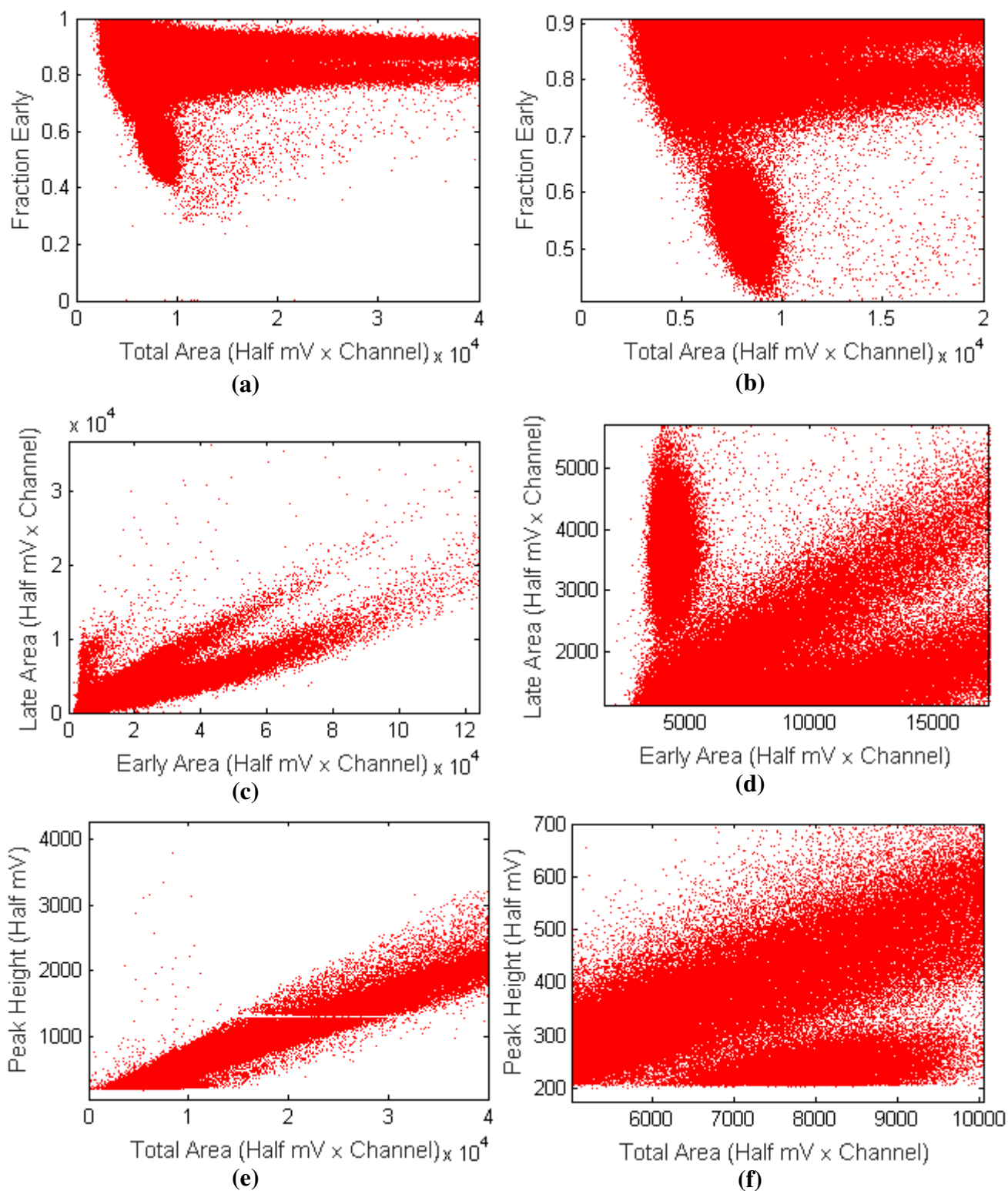


Figure 3.1 Plots of (a) Fraction Early vs. Total Area, (c) Late Area vs. Early Area, and (e) Peak Height vs. Total Area for ^{252}Cf using EJ-325UV. Plots (b), (d), and (f) are insets of (a), (c), and (e) respectively. Observing the insets demonstrates that distinct regions form in plots of the parameters found to contribute most to the variance.

to neutron interactions in the liquid scintillator and capture pulses from the lithium glass in the fraction early versus total area and the late versus early area plot. Separation between gammas and neutron is visible in all three. Thus Fig. 3.1 visually confirms the results of the eigenvector analysis. Note that the regions are more distinct when the individual figures are larger than shown here.

The eigenvector matrix was then applied to the matrix of parameters as a rotation matrix. Fig. 3.2 plots the first and second principal axes of the data. Upon inspection, the visual separation appears to be worse than before (see Fig. 3.1). The data have been rotated in the directions of greatest variance, resulted in stretched out regions that fail to improve the ratios of confirmed neutrons and misidentified gammas to the total number of events detected. This behavior was consistent throughout the analysis of each dataset.

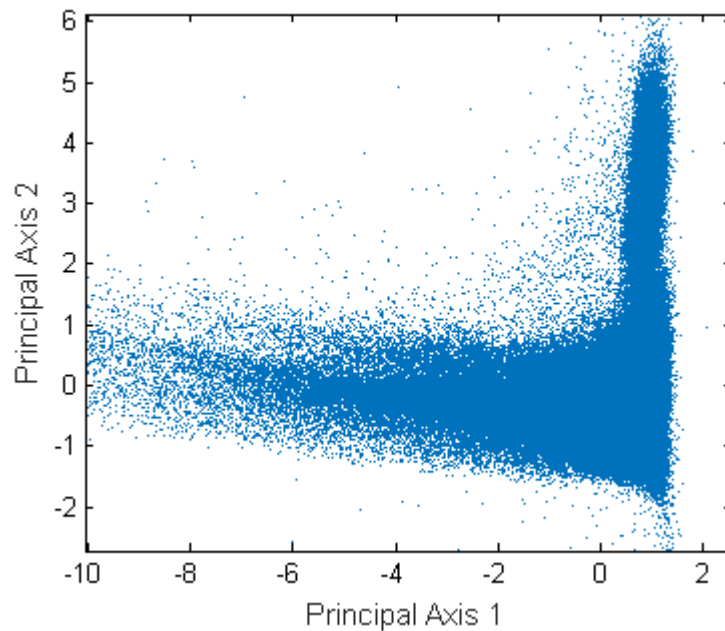


Figure 3.2 PSD parameters of ^{252}Cf rotated onto the 1st and 2nd principal axes. There is no improvement after the analysis in visual separation of the regions (see Fig. 3.1 for comparison)

3.1.2 Feature and Fisher weighting

In order to determine distinguishing parameters of the liquid scintillator and the lithium glass neutron regions, I performed feature and Fisher weighting. Fig. 3.3a displays the regions selected for this analysis. Note that these are similar to the regions in Fig. 2.5, but are slightly different due to the error inherent in selecting the regions. Table 3.2a contains the feature and Fisher weights corresponding to the regions. The larger values indicate the most important features in distinguishing between the two regions; unsurprisingly, fraction early has the largest weight. The lithium neutron region lies below the liquid neutron region in Fig. 3.3a; thus the weight quantifies the visual separation already seen in the plot. The next most significant parameter is the after-peaking parameter, which again is unsurprising, as the after-peaking parameter has shown to distinguish well between lithium and liquid neutrons. The same pattern is seen in the Fisher

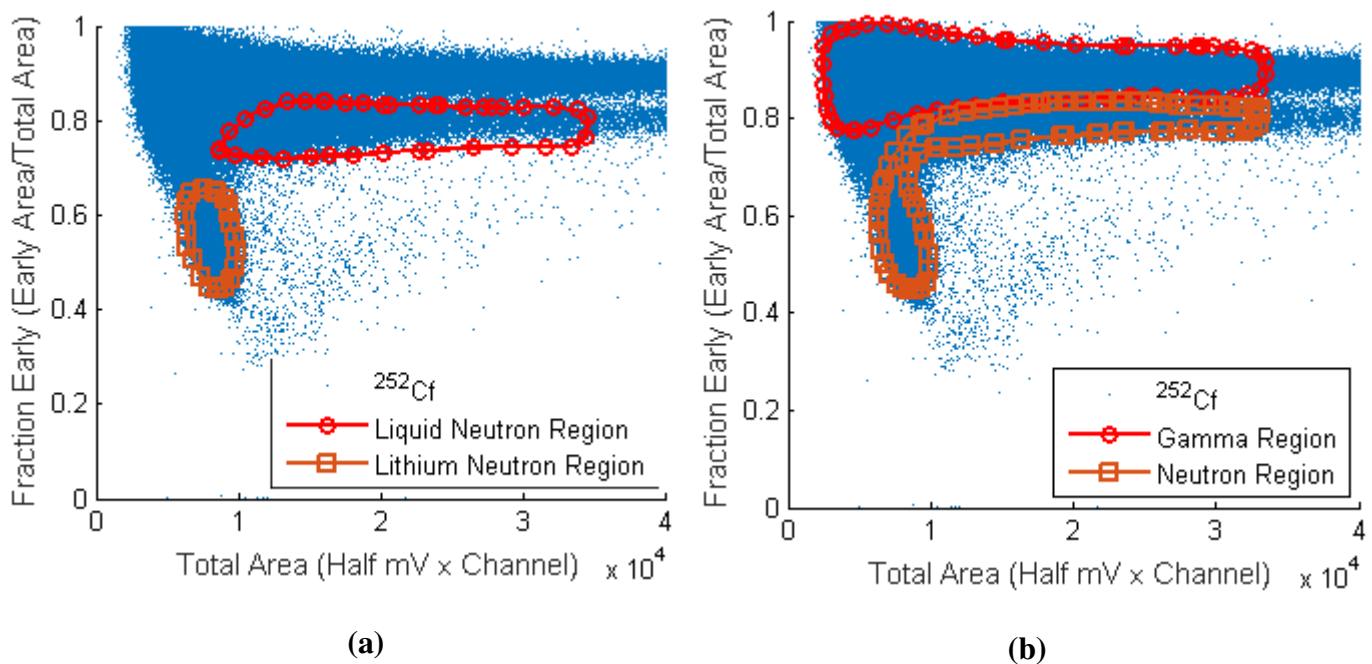


Figure 3.3 Reference regions to compare (a) liquid neutron pulses to lithium neutron pulses and (b) gamma pulses to neutron pulses in either scintillator. Note that the overlap region was avoided in order to emphasize the characteristics of the known regions.

weights, but with much smaller values.

I also analyzed the gamma region versus the liquid and lithium neutron regions combined. Fig. 3.3b indicates the regions selected; there is some inclusion of the gap between the circular lithium region and the liquid region as to remain cohesive. Table 3.2b contains the weights pertaining to this analysis. In this analysis, the fraction early does not prove to be as strong of an indicator for PSD. Instead, late area is the dominating parameter, followed by the fraction early and the after-peaking parameter. Again, the Fisher weights follow the same trend, but remain much smaller in value, reducing the significance of the difference.

In the case of the lithium neutron region and liquid neutron region comparison, I applied the feature weights to the data and applied principal component analysis. Table 3.3 contains the resulting eigenvalues and eigenvectors. Comparison with Table 3.1 demonstrates the effect of the

Table 3.2 Feature and Fisher weights for (a) liquid neutron pulses compared to lithium neutron pulses and (b) gamma pulses to neutron pulses from either scintillator. The weights are larger in (a) because the lithium region is the most distinct of the regions, while in (b) the difference in the parameters for gamma pulses and liquid neutrons pulses is not significant enough to produce large weights. Also note that the Fisher weights are much smaller, thus producing lesser effects when applied to the data.

(a)							
Weight	F_E	A_T	P_H	W	A_L	A_E	A_P
Feature	51.19	6.199	9.132	7.091	2.031	8.641	17.11
Fisher	12.71	1.412	2.161	1.704	0.0849	2.036	4.263

(b)							
Weight	F_E	A_T	P_H	W	A_L	A_E	A_P
Feature	9.106	2.065	2.091	4.038	11.37	2.025	4.376
Fisher	1.810	0.1347	0.1585	0.7658	2.480	0.0829	0.7514

weighting on the outcome of the analysis. The variance shifts heavily towards the first eigenvector, which contains 85% of the total variance of the system alone, and 94% of the variance is contained in the first two principal axes. The loadings indicate that the variance shifted heavily towards the fraction early and the after-peaking parameter due to the increased weight on those parameters.

Table 3.3 Eigenvalues (λ_i) and Eigenvectors (ξ_i) from principal component analysis of data weighted using the feature weights in Table 3.2a. Comparison with Table 3.1 reveals that the variance was shifted towards the parameters with the largest weights, and that the variance is concentrated even more in the first two ξ_i .

(a) Eigenvalues

	λ_1	λ_2	λ_3	λ_4	λ_5	λ_6	λ_7
λ_i	1.35×10^8	1.42×10^7	8.10×10^6	1.54×10^6	1.01×10^5	2.30×10^4	49.4
$\lambda_i / \sum_{i=1}^N \lambda_i$	0.849	0.0894	0.0510	9.71×10^{-3}	6.33×10^{-4}	1.45×10^{-4}	3.11×10^{-7}

(b) Eigenvectors

Loadings	ξ_1	ξ_2	ξ_3	ξ_4	ξ_5	ξ_6	ξ_7
A_T	-6.48×10^{-3}	-0.223	0.384	0.0107	-0.443	0.0857	0.774
F_E	-0.986	0.151	0.0671	-6.50×10^{-3}	-3.95×10^{-3}	-1.94×10^{-3}	-1.84×10^{-5}
P_H	-0.0208	-0.359	0.527	0.0899	0.540	-0.542	2.16×10^{-3}
W	0.0476	0.179	0.207	-0.958	0.0620	-0.0167	-1.11×10^{-4}
A_L	7.27×10^{-3}	-0.0343	0.125	-0.0149	-0.705	-0.562	-0.413
A_E	-0.0167	-0.331	0.514	0.0307	-0.106	0.678	-0.481
A_P	0.156	0.810	0.497	0.268	0.0313	0.0166	3.61×10^{-5}

3.2 Correlated pulses

As described in Chapter 2, correlated pulses were sought among the events detected. Fig. 2.8 is an example of a declared neutron event. The first pulse in the neutron event matches the liquid scintillator neutron event while the second matches a lithium glass neutron event. The first pulse decays more quickly than the second pulse and is followed by less after-peaking, yet the tail and after-peaking are sufficient to distinguish the pulse from that of a gamma ray, which are much sharper in time than neutron pulses. The second pulse has significant after-peaking and a slower decay time, creating the larger tail expected of a lithium glass capture pulse. Note that the pulse height of a liquid scintillator neutron pulse varies significantly based upon the neutron energy, while all the lithium capture pulses are of similar height. This is due to the nature of the interactions, in which the liquid pulse heights are related to the energy lost in the collisions, while the capture pulse height is related to the binding energy of the neutron.

The algorithm for classifying neutron events uses both the liquid pulse-gated and the lithium pulse-gated method. Both methods significantly reduced the number of events described as neutrons, lowering the ratio of misidentified gammas by up to two orders of magnitude. However, this also resulted in neutron detection efficiencies below 1%. Table 3.4a contains the calculated efficiencies for both correlation methods for the EJ-325UV detector, while Table 3.4b reports the calculated efficiencies of the EJ-325a detector. Due to the many decay paths of radium, we were unable to characterize our source through the source's activity on a reference date and its half-life. However, as aforementioned, the sources were placed such that the count rates were nearly equivalent, as can be seen in Table 3.4a and Table 3.4b, and the radium and cobalt sources were at the same distance from the detector. Therefore, radium efficiency calculations were performed using the cobalt activity rate, and should be taken as rough approximations only. Theoretical efficiencies for the background radiation were not calculated, as no counts were declared neutrons by either method (see Table 3.4a and Table 3.4b).

Table 3.4 The calculated absolute and relative efficiencies using the correlated-pulse analysis of the EJ-325UV (a) and EJ-325a (b) detector. Method indicates if the lithium pulse-gated or liquid pulse-gated method was used; n_{exp} is the number of events classified neutrons, N_{exp} is the total number of events detected, $\frac{\Omega}{4\pi}$ is the ratio of the solid angle to 4π steradians, N_{theory} is the theoretical number of particles that interacted with the detector, ϵ_{abs} is the absolute efficiency and ϵ_{rel} is the relative efficiency. Note that these ratios represent gamma rays misidentified as neutrons for the ^{60}Co and Ra sources.

(a)							
Source	Method	n_{exp}	N_{exp}	$\frac{\Omega}{4\pi}$	N_{theory}	ϵ_{abs}	ϵ_{rel}
^{252}Cf	Lithium	382	347717	8.92×10^{-3}	917855	4.16×10^{-4}	1.10×10^{-3}
^{252}Cf	Liquid	207	347717	8.95×10^{-3}	921843	2.25×10^{-4}	5.95×10^{-4}
Background	Lithium	0	73487	N/A	N/A	N/A	0
Background	Liquid	0	73487	N/A	N/A	N/A	0
^{60}Co	Lithium	7	347715	3.35×10^{-2}	3748416	1.87×10^{-6}	2.01×10^{-5}
^{60}Co	Liquid	5	347715	3.32×10^{-2}	3715731	1.35×10^{-6}	1.44×10^{-5}
Ra	Lithium	16	348230	3.37×10^{-2}	3762233	4.25×10^{-6}	4.59×10^{-5}
Ra	Liquid	6	348230	3.33×10^{-2}	3717552	1.61×10^{-6}	1.72×10^{-5}
(b)							
Source	Method	n_{exp}	N_{exp}	$\frac{\Omega}{4\pi}$	N_{theory}	ϵ_{abs}	ϵ_{rel}
^{252}Cf	Lithium	278	345675	8.95×10^{-3}	916381	3.03×10^{-4}	8.04×10^{-4}
^{252}Cf	Liquid	172	345675	8.99×10^{-3}	920353	1.87×10^{-4}	4.98×10^{-4}
Background	Lithium	0	68606	N/A	N/A	N/A	0
Background	Liquid	0	68606	N/A	N/A	N/A	0
^{60}Co	Lithium	4	345208	3.37×10^{-2}	3753671	1.07×10^{-6}	1.16×10^{-5}
^{60}Co	Liquid	2	345208	3.30×10^{-2}	3676090	5.44×10^{-7}	5.80×10^{-6}
Ra	Lithium	13	345315	3.32×10^{-2}	3699120	3.51×10^{-6}	3.76×10^{-5}
Ra	Liquid	9	345315	3.31×10^{-2}	3695381	2.44×10^{-6}	2.61×10^{-5}

Table 3.4a also shows the increased success of the lithium pulse-gated method. Selecting neutrons by searching for the lithium capture pulse first results in 85% more neutrons than searching for pulses in the known liquid scintillator neutron region first when using EJ-325UV. The improvement is less pronounced in the EJ-325a results. Table 3.4b shows a 62% increase in declared neutrons for the ^{252}Cf datasets. For both scintillators, however, the increased neutron detection efficiency comes with an increase in misidentified cobalt gammas, with a 40% increase for EJ-325UV and a 50% increase for EJ-325a. Despite the increase, the ratio of misidentified cobalt gammas to declared californium neutrons decreases to 1.8% from 2.4% when using the lithium capture gated method for EJ-325UV; the ratio increases from 1.1% to 1.4% for EJ-325a.

Comparison of the EJ-325a and EJ-325UV results show that the EJ-325a efficiencies for the ^{252}Cf and the misidentified gamma ratios for the ^{60}Co are lower than those of the EJ-325UV. Using the lithium pulse-gated method, the absolute efficiency for is 37% higher and the misidentified gamma ratio is 75% higher. If the number of confirmed neutrons is used instead to compare the scintillators, the percent increases are identical. However, these values are highly sensitive to the region selected. I always attempted to select identical regions when calculating the values, but there is always some variation. Other regions have resulted in increases of only 23% for the absolute efficiency and 59% for the misidentified gammas.

3.3 Analysis

Principal component analysis and feature and Fisher weighting provide information regarding which parameters contain the variance in the data and therefore indicate which plots can be used to distinguish neutron and gamma events. Generally speaking, feature weighting is more useful than Fisher weighting, as there is greater variation in the values of the feature weights than there is in the Fisher weights. However, we can see that the large values are not much larger than their

fellows, indicating that while there is variance due to those parameters, it is not large. When the data are rotated in the direction of greatest variance (either with or without the weights), we fail to see improved visual separation. This weakens the utility of PCA and feature and Fisher weighting in PSD, though the weights, along with the loadings of the eigenvectors, do quantify the significance of each parameter's contribution to the variance. We found that the total area, after-peaking parameter, fraction early, peak height, and late area were the greatest factors pertaining to distinguishing pulses. Therefore, we expect that plotting these features against one another should provide good region separation, as seen in Fig. 3.1.

Correlated-pulse analysis greatly diminishes the probability of a gamma ray being misidentified as a neutron, but at the cost of greatly eliminating the efficiency of detecting neutrons. The calculated efficiency using the ^{252}Cf source dropped below 1%, while the efficiency using single-pulse analysis ranges from 10-30%, depending upon the region selected. This implies that the detector could be used in two different operating modes: one utilizing correlated-pulse analysis to determine if an unknown source is a neutron source, the second utilizing single-pulse analysis to obtain as much information as possible about a known neutron source. The correlated-pulse mode of operation would therefore be used first on an unknown source in order to determine if the source should be analyzed using the single-pulse mode of operation. Having two modes of operation greatly extends the possible uses of this detector, and having a single PMT increases its potential as it could be easily moved to different locations.

We also found the efficiencies to be higher using the lithium pulse-gated method than the liquid pulse-gated method. This is expected, as the lithium pulse-gated method takes into account the overlap region in order to obtain more information on low-energy neutrons. This comes with the cost of higher misidentified gamma ratios; however, the ratios of misidentified gamma counts from ^{60}Co to the neutron counts from ^{252}Cf for the lithium pulse-gated method are below 2% for both detectors, indicating there is still a significant discrepancy between gamma sources and neutrons

sources when considering the number of events classified as neutrons.

Comparing EJ-325UV to EJ-325a shows that the EJ-325UV detector identifies 20–40% more neutrons from ^{252}Cf than the EJ-325a detector. The variation in the percentage is dependent upon the region selected, which suffers from the nature of the region selection method. Still, the results indicate that there may be significant absorption of light in the EJ-325a scintillator due to the wavelength-shifting phosphor. Therefore, information from the lithium-6 glass may be lost in that detector. However, a definite conclusion cannot be drawn until further statistical analysis is performed, as it is unclear if the increased efficiencies are statistically significant. Correlated-pulse analysis was only performed on one dataset per source for each detector, so additional data are needed to have more points of comparison.

3.4 Conclusions

In this work, we found that PCA and feature and Fisher weighting fail to conclusively improve PSD in single-pulse analysis. The loadings of the eigenvectors and the feature and Fisher weights do quantify the contributions of the PSD parameters to the overall variance and the variance between different pulse regions. This analysis shows that the total area, after-peaking parameter, fraction early, peak height, and late area were the greatest factors pertaining to distinguishing pulses. Consequently, fraction early versus total area, peak height versus total area, and late area versus early area are combinations that provide good region separation, particularly when combined with the after-peaking parameter.

The correlated-pulse analysis improves the misidentified gamma rays ratios by up to two orders of magnitude from the single-pulse analysis, giving ratios around $1 \times 10^{-4}\%$; however the neutron efficiency drops below 1% as a result, while the single-pulse analysis results in efficiencies of 10–30%. The performance of the detector under different modes of operation suggests that

the correlated-pulse mode be used to identify possible neutron sources and that the single-pulse analysis be used to examine known neutron sources. The lithium pulse-gated method produces efficiencies 60–85% larger than the liquid pulse-gated method. This is due to the inclusion of the overlap region in the calculations. We are confident that the events in the overlap region are neutrons from the lithium pulse found in the event. The increase in the misidentified gamma ratio by 40–50% does not hinder the detector’s ability to distinguish between between neutron and gamma sources, as the ratio of misidentified gammas to classified neutron events is largely unchanged using both methods.

Absorption of light from the lithium-6 glass in the EJ-325a may be significant, as the EJ-325UV detector identifies 20–40% more neutrons than the EJ-325a detector. We cannot conclude this definitively; more statistical analysis is needed to determine the statistical significance of the increased number of identified neutrons, and more data are necessary in order to perform that analysis.

3.5 Further work

Future explorations into the self-absorption of the EJ-325a detector require additional statistical analysis to analyze the significance in the increased neutron counts in the EJ-325UV. The percentages calculated were all from the same data, but with slightly different regions each time the calculations were performed. In order to perform a variance test, we would need to replicate the experiment several times, calculate the percentages, and perform the analysis of variance (ANOVA) test. The result of this test would give us more insight into the significance of self-absorption in our detector.

Another important consideration is room return. Our sources were placed close to or on the concrete floor of our lab. Proximity to the walls greatly increases room return, and therefore many

of the events observed may not be neutrons directly from the source in question. One way to eliminate room return is to perform measurements high off the ground. The BYU Nuclear Physics Group owns a lift for such experiments; however, our detector was not designed to be light-tight, as experiments were performed inside of a light-tight wooden box. A new detector container would need to be created to accommodate the detector so it could be placed on the lift and used without damaging the PMT. This would also eliminate the wooden box as a source of concern, as the high hydrogen content of the wood adds to the room return as well.

Another factor to explore is the length and amount of argon bubbling. Our container is not air-tight, allowing the argon to slowly escape over time and oxygen to mix with the liquid scintillator. As mentioned, the regulator was meant for much larger flow rates, so it was difficult to actually calculate the volume of argon bubbled into the scintillator. If a regulator meant for lower flow rates could be obtained, more accurate measurements of argon volume could be made. Then the optimum amount of argon bubbling may be determined by examining how the PSD capabilities of the scintillator change with different argon volumes. Also, experiments can be conducted to determine how long the detector will maintain its PSD capabilities after bubbling in the container that is not air-tight. Design of an air-tight container would serve to increase that effective lifetime of the detector.

The hybrid detector should also be explored using other liquid organic scintillators. We chose EJ-325 due to the lack of safety concerns, thus facilitating its use, but other liquid scintillators such as EJ-301 are known to possess much greater PSD capabilities. This could possibly increase the reliability of our results by increasing the separation between the gamma region and the liquid neutron region. Care would need to be taken in order to design a container that could keep out oxygen, once bubbled with argon or nitrogen, to reduce combustion risk. However, the benefits may very well outweigh the difficulty in preparing such a container.

Following researchers should also consider adjusting the correlated-pulse algorithm to include

other pulse shape parameter plots. Only fraction early versus total area and the after-peaking parameter were considered in determining whether or not two pulses were correlated or not; however, it was shown that late area versus early area also produces good PSD, and it even demonstrates separate liquid and lithium-6 neutron regions. Thus other parameters could be used either separately or together with the existing algorithm in order to find the optimal PSD method for this detector.

Bibliography

- [1] G. F. Knoll, Radiation detection and measurement, John Wiley & Sons, 2000.
- [2] D. A. Shea, D. Morgan, The helium-3 shortage: Supply, demand, and options for congress, Congressional Research Service, Library of Congress, 2010.
- [3] E. Technology, Ej-325a mineral oil based liquid scintillator with n- γ PSD property, <http://www.eljentechnology.com/index.php/products/plastic-scintillators/115-ej-325a>, Accessed 10 February 2016.
- [4] A. S. Technologies, Li doped glass scintillators, http://www.apace-science.com/ast/g_scint.htm, Accessed 10 February 2016.
- [5] A. Dalton, Measurement of the responses of small lithium glass scintillators to protons, deuterons and alpha particles, Tech. rep., CM-P00067990 (1987).
- [6] T. Jex, Preliminary study of a dual PMT lithium-cadmium hybrid neutron detector, B.S. Thesis, Brigham Young University, Provo, UT, 2014.
- [7] L. B. Rees, J. B. Czirr, [Optimizing moderation of He-3 neutron detectors for shielded fission sources](#), Nuclear Instruments and Methods in Physics Research Section A: Accelerators, Spectrometers, Detectors and Associated Equipment 691 (2012) 72 – 80. doi:[http:](http://)

[//dx.doi.org/10.1016/j.nima.2012.07.004](http://dx.doi.org/10.1016/j.nima.2012.07.004).

URL <http://www.sciencedirect.com/science/article/pii/S0168900212007516>

- [8] A. Comrie, A. Buffler, F. Smit, H. Wörtche, Digital neutron/gamma discrimination with an organic scintillator at energies between 1 MeV and 100 MeV, *Nuclear Instruments and Methods in Physics Research Section A: Accelerators, Spectrometers, Detectors and Associated Equipment* 772 (2015) 43–49.
- [9] M. Divadeenam, J. Stehn, [A least-squares fit of thermal data for fissile nuclei](#), *Annals of Nuclear Energy* 11 (8) (1984) 375 – 404. doi:[http://dx.doi.org/10.1016/0306-4549\(84\)90002-1](http://dx.doi.org/10.1016/0306-4549(84)90002-1).
URL <http://www.sciencedirect.com/science/article/pii/0306454984900021>
- [10] E. Browne, J. Tuli, [Nuclear data sheets for A = 60](#), *Nuclear Data Sheets* 114 (12) (2013) 1849 – 2022. doi:<http://dx.doi.org/10.1016/j.nds.2013.11.002>.
URL <http://www.sciencedirect.com/science/article/pii/S0090375213000823>
- [11] C. Higgins, Cadmium capture-gated neutron detector analysis of the ^{235}U fission spectrum, B.S. Capstone, Brigham Young University, Provo, UT, 2014.
- [12] G. Hill, Single pulse neutron and gamma discrimination with combination glass and liquid hybrid detector, B.S. Thesis, Brigham Young University, Provo, UT, 2016.
- [13] E. Technology, Ej-301 liquid scintillator, <http://www.eljentechnology.com/index.php/products/liquid-scintillators/71-ej-301>, Accessed 10 February 2016.
- [14] X. Hua-Lin, D. Jing-Shan, W. Nai-Yan, Oxygen quenching in a lab based liquid scintillator and the nitrogen bubbling model, *Chinese Physics C* 34 (5) (2010) 571.

-
- [15] M. Martin, [Nuclear data sheets for A = 248](#), Nuclear Data Sheets 122 (2014) 377 – 409.
doi:<http://dx.doi.org/10.1016/j.nds.2014.11.004>.
URL <http://www.sciencedirect.com/science/article/pii/S009037521400670X>
- [16] M. A. Sharaf, D. L. Illman, B. R. Kowalski, Chemometrics, Vol. 82, John Wiley & Sons, 1986.

Index

- α particle, 3, 4
 - decay, 15, 28
- β decay, 5, 15
- After-peaking
 - liquid scintillator neutron interaction, 18, 36
 - lithium-6 neutron interaction, 18, 36
 - parameter, 8, 9, 16–18, 20, 24, 25, 30, 33–35, 39, 40, 43
- Amplifier, 14
 - Ortec, 13
 - settings, 4, 14
- Anthracene, 14
- Applied Scintillation Technologies GS20 lithium-6 glass, 3, 10, 14
- Area
 - Early, 32
 - early, 5, 16, 17, 19, 20, 30, 40, 43
 - late, 5, 16, 17, 19, 20, 30, 32, 34, 39, 40, 43
 - total, 5, 16–20, 24, 30, 32, 39, 40, 43
- Argon, 13, 42
 - bubbling, 13, 42
- Attenuator, 14
- Autoscaling, 19, 20
- Best controller, 15
- Cadmium, 7
- CAEN digitizer, 14, 15
- Californium-252, 5, 9, 15, 16, 23, 28, 38–40
 - average neutrons per fission, 15, 28
 - half-life, 15, 28
- Cerium, 3
- Channel, 16
- Cobalt-60, 5, 9, 16, 28, 36, 39
 - gamma energies, 5
- Detector, hybrid, 8, 9
 - design, 10
 - digital signal recombination, 15
 - equipment, 13
 - signal acquisition, 13–15
 - time window, 23
- Efficiency, 25, 27, 28
 - absolute, 27, 28, 38
 - calculations, 10, 36
 - detector, 27, 36, 38–40
 - of light collection, 13
 - relative, 27
- fluorescence, 3
- Fraction early, 5, 16–20, 24, 25, 30, 33–35, 39, 40, 43
- Gamma ray, 2, 4, 11
 - energy, 5, 16
 - high, 5
 - event, 17, 21
 - interaction, 4, 5
 - misidentified, 9, 28, 36, 38–40
 - pulse tail, 5, 18
 - source, 5, 16
- Helium-3
 - cost, 2
 - portal detector, 2
 - proportional counter, 1
 - shortage, 2
- MatLab, 9, 23

- Moderator, 4, 7
- Neutron, 1, 2, 11
cross section
helium-3, 2
lithium-6, 3
energy, 1, 3, 4, 36
binding, 36
low, 2, 7, 26, 39
event, 17
interaction, 4–6, 22, 32
liquid organic, 9
liquid scintillator, 3, 5
lithium-6, 9
lithium-6 glass, 3–5, 7, 9
helium-3, 1
moderated, 11, 22
pulse tail, 5, 8
source, 5, 15
- Ortec
amplifier, 13
PMT base, 13
power supply, 13
- Oxygen, 13, 42
- Peak height, 5, 25, 36, 40
distribution, 11
parameter, 16, 19, 20, 30
- Peak width
parameter, 16, 18–20
- Phosphor
wavelength-shifting, 9, 12, 40
- Photomultiplier tube, 2, 4, 7, 8, 11, 12, 39, 42
Adit, 13
base, 13
- Principal component analysis, 9, 19, 21, 22, 29, 34, 38, 40
axes, 19, 20, 32, 35
correlation matrix, 20, 29
eigenvalue, 20, 29, 34
eigenvector, 20, 29, 32, 34
eigenvector loadings, 30
- PSD primary factors, 30
variance, 19, 20, 32, 39, 40
- Pulse, 9
correlated pulses, 15, 22, 23, 26, 36
analysis, 9, 19, 22, 36, 39, 40, 42
liquid pulse-gated method, 24, 39, 41
lithium pulse-gated method, 25, 38, 39, 41
reference run, 23, 24
recoil, 2
single, 15
analysis, 16, 19, 22, 23, 39, 40
data, 19
tail, 4, 5
- Pulse shape discrimination, 5, 6, 8, 9, 11, 13, 16, 19, 20, 34, 39, 40, 42, 43
algorithm, 16
gamma region, 6, 19, 25, 34
liquid neutron region, 8, 19, 22–25, 33, 34, 36, 38, 43
lithium neutron region, 8, 19, 22–24, 33, 34, 36, 38, 43
neutron pulse origin, 19
neutron region, 6
parameters, 5, 8, 16–20, 33, 34, 38, 39, 43
regions, 8
- Radioactive sources, 5, 15
- Radium, 9, 16, 28, 36
half-life, 36
- Scintillator, 2, 4, 12
liquid organic, 3, 4, 6–9, 12–14, 18, 42
EJ-301, 12, 42
EJ-325, 42
EJ-325a, 3, 8, 9, 11, 12, 14, 36–38, 40, 41
EJ-325UV, 3, 9, 11, 12, 36–38, 40, 41
pulse tail, 5
lithium-6 glass, 3, 4, 6–8, 14, 18
energy band, 3
pulse tail, 5
organic, 4

-
- plastic, 7
 - Self-absorption, 9, 12, 41
 - Solid angle, 27

 - Terminator, 14
 - Trigger, 15, 23
 - threshold, 15

 - Weighting
 - feature, 9, 21, 22, 33, 38, 40
 - Fisher, 9, 21, 22, 33, 38, 40
 - parameter variance weight, 21, 22
 - variance
 - intercategory, 21
 - intracategory, 21, 22